Journal of ELECTRONIC MATERIALS, Vol. 48, No. 4, 2019
https://doi.org/10.1007/s11664-018-06839-3

TOPICAL COLLECTION: INTERNATIONAL CONFERENCE ON THERMOELECTRICS 2018

ZnO-Nanoparticle-Dispersed $Cu_{11.5}Ni_{0.5}Sb_4S_{13-\delta}$ Tetrahedrite Composites with Enhanced Thermoelectric Performance

FU-HUA SUN,[1] JINFENG DONG,[1] HUAICHAO TANG,[1] HUA-LU ZHUANG,[1] and JING-FENG LI [1,2]

1.—State Key Laboratory of New Ceramics and Fine Processing, School of Materials Science and Engineering, Tsinghua University, Beijing 100084, People's Republic of China. 2.—e-mail: jingfeng@mail.tsinghua.edu.cn

$Cu_{12}Sb_4S_{13}$ tetrahedrite is an abundant natural that is also environmentally friendly. There have been efforts made to reach a unity of ZT value through optimizing the interdependence of electrical and thermal performance. In this study, we reported on ZnO nanoparticles-dispersed $Cu_{11.5}Ni_{0.5}Sb_4S_{13-\delta}$ composites that were synthesized by the mechanical alloying and spark plasma sintering method. The structural characterizations were conducted via scanning electron microscopy, electronic probe microscopic analysis and transmission electron microscopy. The ZnO-nanoparticles were uniformly distributed in the $Cu_{12}Sb_4S_{13}$ grains. ZnO was used as a heterogeneous nucleation site to reveal the effectiveness of reducing thermal conductivity, likely derived from the strong low/mid-frequency phonon scattering. The lowest lattice thermal conductivity, 0.33 W m^{-1} K^{-1}, was obtained at 673 K in 0.5 vol.% of ZnO sample. A small quantity of ZnO addition led to a high $ZT \sim 1.0$ at 723 K, which increased by $\sim 42\%$ in the pure-phased $Cu_{12}Sb_4S_{13-\delta}$ sample.

Key words: Thermoelectric, tetrahedrite, ZnO, mechanical alloying

INTRODUCTION

Thermoelectric (TE) materials have attracted great attention for their potential in energy conversion, power generation and electric cooling, due to their significant merits with rapid response times, no noise or vibrations, and ability for remote operation.[1–3] The conversion efficiency of the TE device is related to the materials' dimensionless figure merit of ZT, defined as $ZT = S^2\sigma T/\kappa$, where S is the Seebeck coefficient, σ is the electrical conductivity, κ is the thermal conductivity, and T is the absolute temperature. To obtain a high TE performance, researchers focus on decoupling the dependence of the electrical and thermal transport property.[4–7] Most good studies relied on reducing the lattice thermal conductivity (κ_{lat}) through nano-engineering while simultaneously maintaining a high power factor ($S^2\sigma$, PF).[8,9] One promising approach proposed to enhance phonon scattering by introducing nanoparticles (NPs) into the matrix.[10–13]

Although nanocomposites received significant results in various research fields,[14,15] they are more or less overlooked within thermoelectric tetrahedrites.[16] $Cu_{12}Sb_4S_{13}$ (CAS) is a promising TE material that is a cost-effective element.[17–20] A range of single- or co-substituted CAS compounds have been investigated and have obtained a relatively high ZT value.[21–24] NPs dispersion is an effective procedure in reducing κ_{lat}, so it is feasible that through introducing NPs in a CAS matrix would further enhance the TE performance. The nanocomposites are advantageous for improving the TE performance as they have no effluence of chemical compositions on the host matrixes, they are easy to control, and have good chemical stability even at high temperatures.

(Received July 17, 2018; accepted November 26, 2018; published online December 4, 2018)

In this study, a series of ZnO NPs-dispersed $Cu_{11.5}Ni_{0.5}Sb_4S_{13-\delta}$ composites (CNAS-*x*ZnO) were synthesized using a mechanical alloying and spark plasma sintering (MA + SPS) method. The ZnO NPs were uniformly distributed into the CAS grains, and nanopores were observed after the SPS treatment. The electrical transport property slowly decreased, due to the additional electrons contribution from *n*-type ZnO NPs, although the thermal conductivity reduced as ZnO NPs dispersed. A small quantity of ZnO dispersion (0.5 vol.%) led to a high *ZT* value 1.0 at 723 K, which derived from the large low/mid-frequency defects (including nanoparticles, nanopores and interfaces) phonon scattering.

EXPERIMENTAL PROCEDURES

The experiments began with Sb shots (99.99%) and Cu (99.9%), Ni (99.9%), S (99.99%) and ZnO (99.99%) powders, which were purchased from Aladdin Industrial Corporation (China). These raw materials were weighed in nominal compositions of $Cu_{11.5}Ni_{0.5}Sb_4S_{12.7}$ − *x* vol.% ZnO (*x* = 0.1, 0.2, 0.5, 1.0 and 1.5, abbreviated as CNAS-*x*ZnO) in a dry argon-filled glove box, loaded into a stainless steel vial filled with inert gas, and then subjected to MA at 450 rpm for 10 h in a planetary ball mill. The MA-derived powders were subsequently placed into a 12 mm diameter graphite die, sintered into disks by SPS (SCM-1000-1, Fuji Electronic Industrial Co. LTD., Japan) at 723 K for 10 min in vacuum under an axial pressure of 50 MPa, and then cooled down to room temperature (RT) at a cooling rate of 15 K min^{-1}. A series of ZnO NPs dispersed CNAS-*x*ZnO bulks with a high relative density (above 95%) were fabricated.

The phase identification of the SPSed CNAS-*x*ZnO samples was performed by x-ray diffraction (XRD, D8 Advance, Bruker, Germany) with Cu K_α radiation. The data was collected using 4° min^{-1} over an angular range between 15° to 65° with a step increment of 0.02°. The elemental distribution of the surface-polished bulks were observed by electronic probe microscopic analysis (EPMA, JXA-8230, JEOL, Japan). The morphology and the crystal structure were performed on field emission scanning electron microscopy (FESEM, JSM-7001, JEOL, Japan) and transmission electron microscopy (TEM, 2100, JEOL, Japan).

The SPSed bulks were cut and polished to investigate the following thermoelectric property. The electrical resistivity (ρ) and the Seebeck coefficient (S) were measured simultaneously using a Seebeck coefficient/electrical resistance measuring system (ZEM-3, Ulvac-Riko, Japan) at temperatures ranging from 303 K to 723 K under partial helium pressure. The thermal diffusivity (D) was conducted using the laser flash model (TC-9000, Ulvac-Riko, Japan). The heat capacity (C_p) was a constant value of 0.45 J g^{-1} K^{-1}. The thermal conductivity (κ_{tot}) was calculated using $\kappa = D\rho C_p$, where ρ was the density measured by the Archimedes method.

RESULTS AND DISCUSSION

The diameters of the ZnO particles ranged from 50 to 200 nm, as shown in Fig. 1a. The SAED in Fig. 1b obtained a hexagonal phase with a space group P63mc, PDF#36-1451. High-resolution TEM (HRTEM, Fig. 1c) showed its major crystal planes

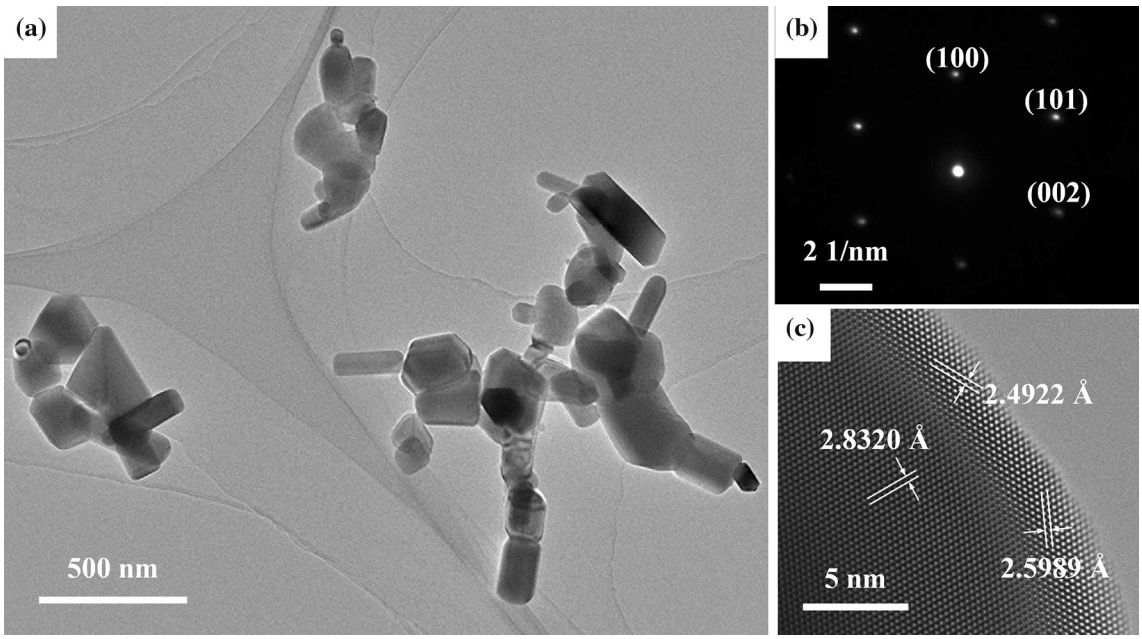

Fig. 1. The images from (a) the transmission electron microscope (TEM), (b) the selected area electron diffraction (SAED), and (c) the high-resolution TEM (HRTEM) for ZnO NPs.

characterized with a defect-free single crystal along the [001] zone axis. The phase structure of the CNAS-*x*ZnO bulks composited with tetrahedrite materials are shown in Fig. 2. A single CAS phase was obtained in the $x < 1.0$ samples, which were indexed to the tetrahedrite phase (PDF#42-0561). No diffraction peak of zinc oxide was detected, due to the low content and good distribution. A new CuS phase (PDF#74-1234) marked with a diamond sign (black diamond) appeared as NPs content exceeded 1.0. That meant that excessive NPs led to the CAS decomposition during the MA + SPS process.

To further confirm the microstructures and the elemental distributions of the CNAS-*x*ZnO composites, the scanning electron microscopy (SEM) and electronic probe microscopic analysis (EPMA) measurements were conducted. As depicted in Fig. 3a, small CNAS grains (~ 0.5 μm) were obtained and characterized with large numbers of nanopores (marked with white dash circles). The Cu, Sb, S, Ni and Zn were homogeneously distributed for the $x = 0.5$ sample seen in Fig. 3b, c, d, e, and f. The ZnO nanoparticles were observed surrounding the CAS grains, as shown in Fig. 4a. The number of nanopores appeared in the triple junctions, as seen in Fig. 3a, which resulted from the different thermal diffusivity between the CAS grains and the ZnO NPs during the SPS treatment. Figure 4b displays the interfaces taken from Fig. 4a (marked with white dash square), which shows a well-bonded interface between the CAS and the ZnO with mismatched orientations. The SAED in Fig. 4c and d displays single crystal diffraction patterns, which correspond to the two major growth orientations of (110), (200) for CAS crystals and (100), (101) for NPs. The fine CAS crystals would cause an improved electrical transport property, where the nanopores and the NPs were effective in reducing thermal conductivity.

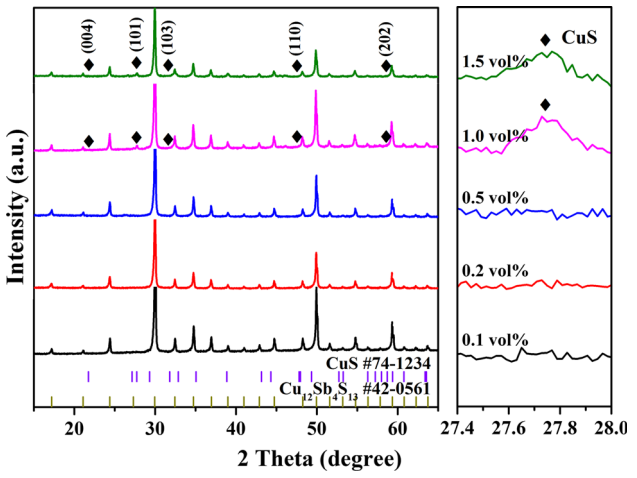

Fig. 2. XRD patterns of the CNAS-*x*ZnO ($x = 0.1$, 0.2, 0.5, 1.0 and 1.5) samples synthesized via a MA + SPS method. The diamond mask (black diamond) indicates the diffraction peaks of the CuS impurity-phase.

Figure 5a shows the temperature-dependent electrical conductivity (σ) of the CNAS-*x*ZnO composites. The σ values had a similar trend throughout the samples, where they initially increased until the mid-temperature region and then decreased. It is a typical property of nondegenerate semiconductors to transfer to metal-like materials. When a small number of NPs were mixed, the σ increased sharply, but slowly decreased as excessive ZnO was added. The *S* values obtained were better than the previous results ($x = 0$ sample, in Fig. 5b).[25] They ranged from 100 μV K^{-1} to 180 μV K^{-1} for CNAS-*x*ZnO composites at temperatures between 323 K and 723 K. The power factors were slowly increased as the NPs content increased, as seen in Fig. 5c. The maximal value was 13.5 μW cm^{-1} K^{-2} for the $x = 0.2$ sample at 723 K.

The total thermal conductivity (κ_{tot}) was low throughout the temperatures, as seen in Fig. 5d. The κ_{tot} values increased slightly as the temperature increased. Dispersing the small NPs content sharply decreased the κ_{tot}. The excessive ZnO NPs remained effective to further reducing the thermal conductivity, so low values, below 0.9 W m^{-1} K^{-1}, were obtained for the $x = 1.5$ sample. This stemmed from the low thermal conductivity of the ZnO and the decomposed CuS phase. We calculated the lattice thermal conductivity (κ_{lat}) by subtracting the carrier contribution (κ_{ele}) from the κ_{tot}. The electrical contribution was estimated by the Wiedemann–Franz relation,[26] $\kappa_{ele} = L\sigma T$, where σ is the electrical conductivity, T is absolute temperature, and L is the Lorenz number obtained via a single parabolic band model. A reduced κ_{lat} was obtained. The lowest κ_{lat} value was 0.33 W m^{-1} K^{-1} for the CNAS-0.5ZnO sample at 673 K. The SEM and TEM images in Figs. 3 and 4 show that these defect centers, including nanoparticles, nanopores, and interfaces were typically introduced to further reduce the κ_{lat} values in the CNAS-*x*ZnO composites. Based on the Debye-Callaway's equation[27]:

$$\kappa_{lat} = \frac{\kappa_B}{2\pi^2 \upsilon}\int_0^{\frac{\kappa_B\theta_D}{\hbar}} \tau_C(\omega)\left(\frac{\hbar\omega}{\kappa_B T}\right)^2 \frac{\omega^2 e^{\frac{\hbar\omega}{\kappa_B T}} d\omega}{\left(e^{\frac{\hbar\omega}{\kappa_B T}} - 1\right)^2}. \quad (1)$$

In this equation, κ_B is the Boltzmann constant, υ is an average phonon-group velocity, θ_D is the Debye temperature, which is obtained from the optimized value in heat capacity calculation, $\hbar$ is the reduced Plank constant, ω is the phonon angular frequency, and T is the absolute temperature, respectively. The κ_{lat} can be expressed as a sum of phonon-scattering contributions with a relaxation time (τ_C) characterized using Eq. 2:

$$\tau_C^{-1} = \tau_{U,N}^{-1} + \tau_D^{-1} + \tau_{GB}^{-1}. \quad (2)$$

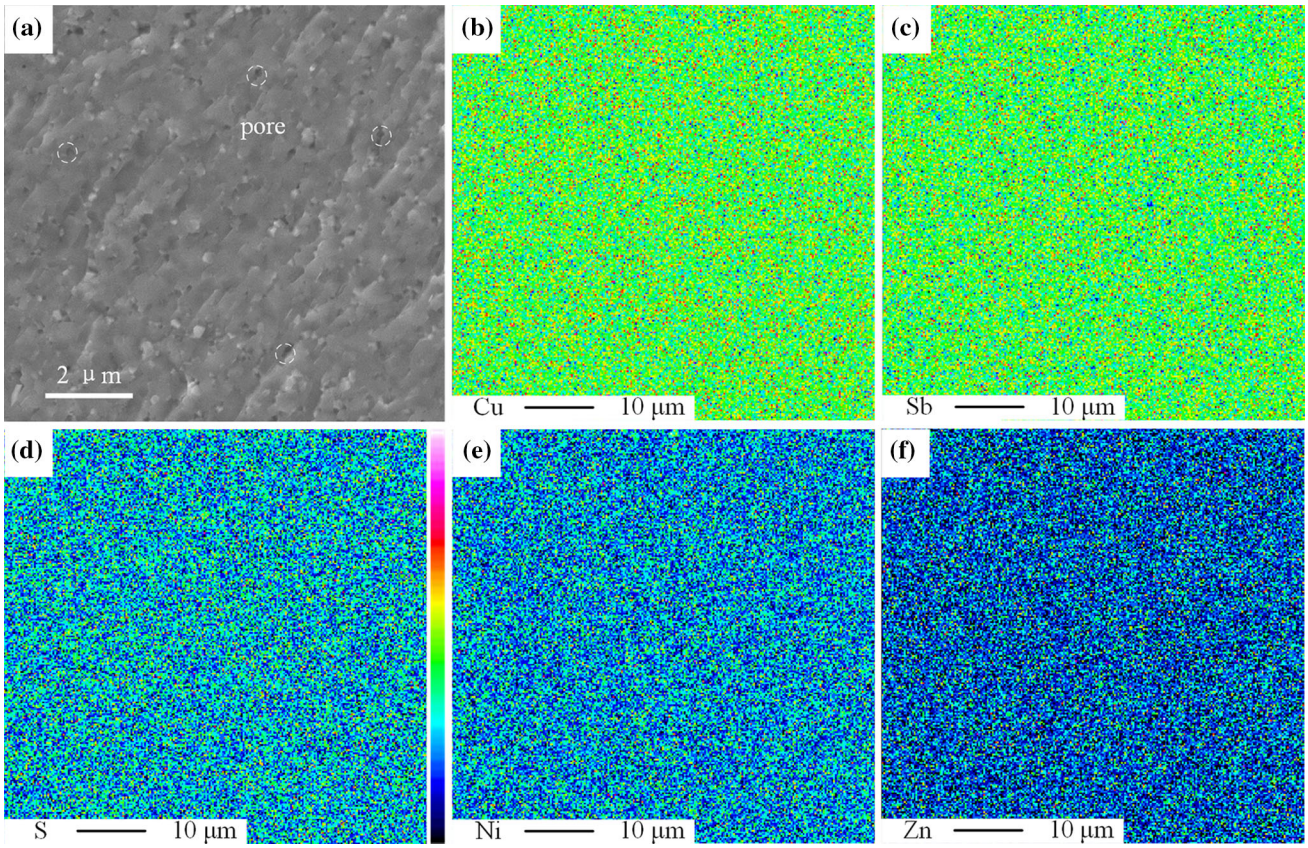

Fig. 3. (a) SEM image of the cracked surface and corresponding EPMA element maps of (b) Cu, (c) Sb, (d) S, (e) Ni, and (f) Zn taken from the polished surface of the CNAS-0.5ZnO sample. The white dash circles are the nanopores.

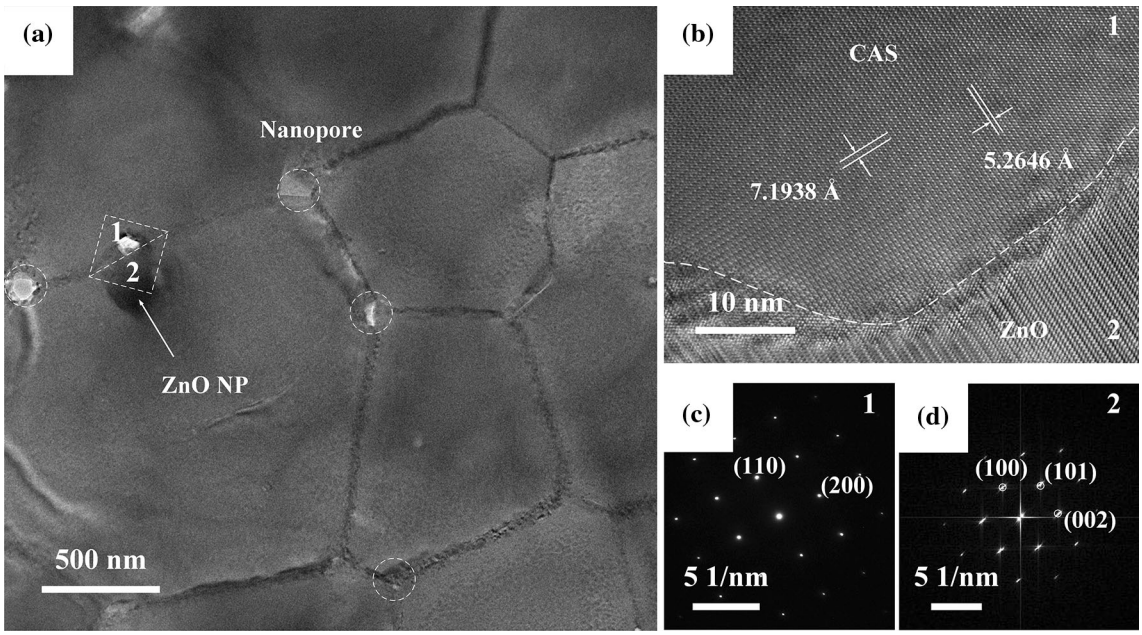

Fig. 4. (a) Low-magnification bright-field TEM image of the CNAS-0.5ZnO sample that shows the nanopores (white dash circles) and the CAS grain boundaries. (b) The CAS interfaces and (c) and (d) the SAED images taken from (a) and marked with Arabic numbers 1 and 2 (white dash square).

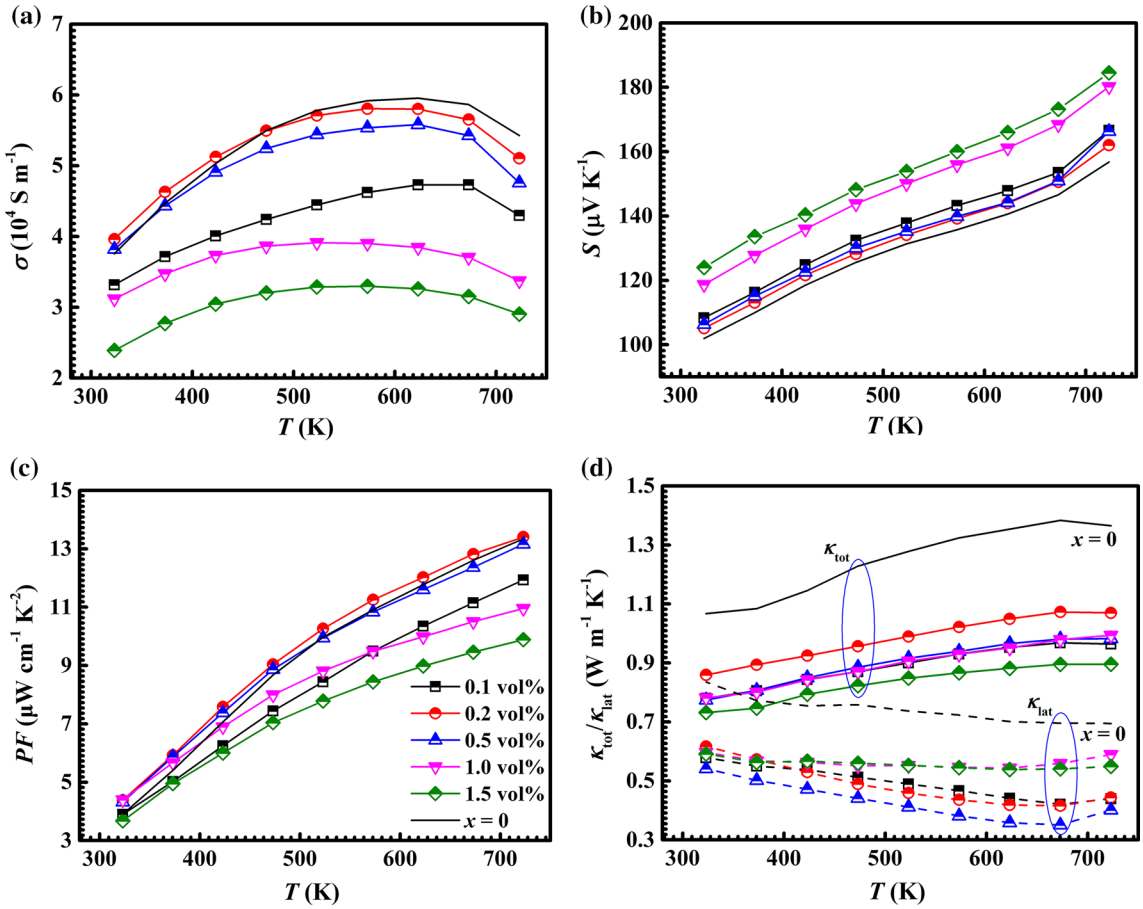

Fig. 5. The temperature-dependence of (a) the electrical conductivity (σ), (b) the Seebeck coefficient (S), (c) the power factor (PF) and (d) the total/lattice thermal conductivity ($\kappa_{tot}/\kappa_{lat}$) for the CNAS-$x$ZnO composites synthesized by a MA + SPS method.

$\tau_{U,N}$ proportional to ω^{-2} is the Umklapp and Normal processes, which are almost the same for all tetrahedrite materials. Here, we introduced ZnO NPs in our composites. The mismatched interfaces between CAS and NP have dislocation phonon scattering to further reduce κ_{lat} values, conducted as a relaxation time $\tau_D \sim \omega^{-1}$ and ω^{-3} targeting mid-range frequency phonons. And the grain boundary contribution of NP ($\tau_{GB} \sim \omega^0$) plays an important role in phonon scattering at the low-frequency end. Therefore, they all largely scattered phonon transport, and then reduced the lattice thermal conductivity, as shown in Fig. 5d. It can clarify the phonon scattering contribution from the ZnO nanoparticles addition.

The improved ZT values were obtained for the CNAS-xZnO composites by combining the PFs with largely reduced thermal conductivity, as shown in Fig. 6a. The maximum $ZT \sim 1.0$ was achieved in the $x = 0.5$ sample at 723 K, which increased by ca. 42% for the pristine CAS. We determined the maximal conversion efficiency (η_{max}) and the average ZT (ZT_{ave}) for the CNAS-0.5ZnO sample. The η_{max} and the ZT_{ave} values were calculated based on a finite difference analysis[28] as follows

$$\eta_{max} = \frac{\Delta T}{T_{hot}} \frac{\sqrt{1 + Z \cdot T_{ave}} - 1}{\sqrt{1 + Z \cdot T_{ave}} + \frac{T_{cold}}{T_{hot}}}, \quad (3)$$

$$ZT_{ave} = \frac{\int_{T_{cold}}^{T_{hot}} ZT(T)\mathrm{d}T}{T_{hot} - T_{cold}}, \quad (4)$$

where T_{hot} and T_{cold} are the hot- and cold-side temperatures, and $\Delta T = T_{hot} - T_{cold}$ and $T_{ave} = (T_{hot} - T_{cold})/2$ are their differences and average. Figure 6b shows that the CNAS-0.5ZnO sample possessed a high ZT_{ave} value of 0.55 accompanied with a high $\eta_{max} \sim 8\%$ at $\Delta T = 400$ K, which indicated a promising MA + SPS technique to synthesize CAS composites with potential to design a thermoelectric device.

CONCLUSIONS

ZnO dispersed $Cu_{11.5}Ni_{0.5}Sb_4S_{13-\delta}$ samples were synthesized via a simple mechanical alloying and spark plasma sintering method. The electrical transport property slowly decreased, but the thermal conductivity was largely reduced as ZnO

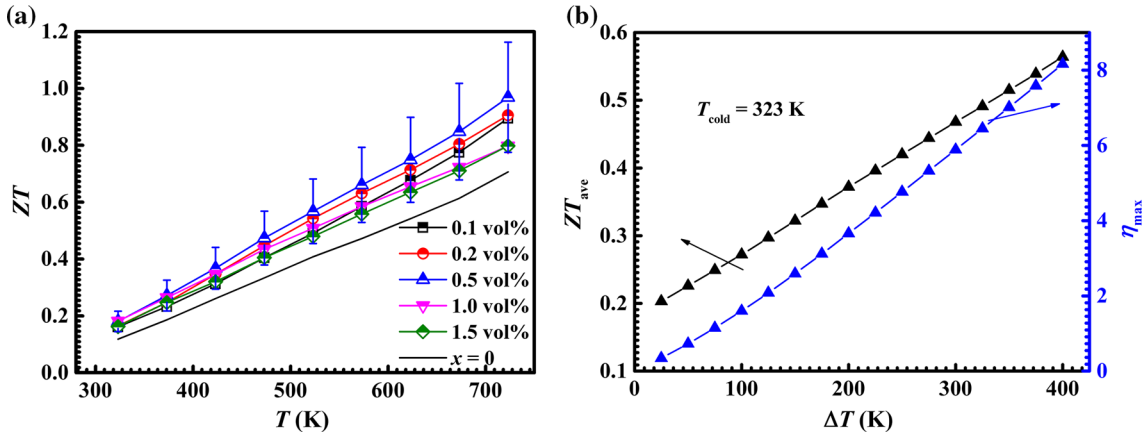

Fig. 6. (a) Figure of merit of the *ZT* dependence on temperature in the CNAS-*x*ZnO composites. The error bars represented 20% uncertainty in the *ZT* values. (b) The average *ZT* (ZT_{ave}) and maximum conversion efficiency (η_{max}) versus temperature difference (ΔT) for the CNAS-0.5ZnO. For η_{max} and ZT_{ave}, a cold side temperature (T_{cold}) was assumed to be 323 K.

nanoparticles dispersed into the $Cu_{11.5}Ni_{0.5}Sb_4S_{13-\delta}$ matrix. The lowest κ_{lat} value was 0.33 W m^{-1} K^{-1} for the CNAS-0.5ZnO sample at 673 K, because of the additional defects-derived scattering for low/mid frequency phonons. A small number of ZnO dispersion ($x = 0.5$) led to a high *ZT* value $\sim$ 1.0 at 723 K, which increased by $\sim$ 42% for the single-phased $Cu_{12}Sb_4S_{13-\delta}$ sample. The CNAS-0.5ZnO sample presented high η_{max} and ZT_{ave} values, indicating the effectiveness of nanostructuring as a promising technique within tetrahedrites toward high thermoelectric conversion efficiency.

ACKNOWLEDGMENTS

This work was supported by National Key R&D Program of China (Grant No. 2018YFB0703603) and the National Natural Science Foundation of China (Grant No. 11474176).

REFERENCES

1. C. Forman, I.K. Muritala, R. Pardemann, and B. Meyer, *Renew. Sustain Energy Rev.* 57, 1568 (2016).
2. Q.H. Zhang, X.Y. Huang, S.Q. Bai, X. Shi, C. Uher, and L.D. Chen, *Adv. Eng. Mater.* 18, 194 (2016).
3. D. Kraemer, Q. Jie, K. McEnaney, F. Cao, W.S. Liu, L.A. Weinstein, J. Loomis, Z.F. Ren, and G. Chen, *Nat. Energy* 1, 1 (2016).
4. L.D. Zhao, G.J. Tan, S.Q. Hao, J.Q. He, Y.L. Pei, H. Chi, H. Wang, S.K. Gong, H.B. Xu, V.P. Dravid, C. Uher, G.J. Snyder, C. Wolverton, and M.G. Kanatzidis, *Science* 351, 141 (2016).
5. J. Shuai, J. Mao, S.W. Song, Q. Zhu, J.F. Sun, Y.M. Wang, R. He, J.W. Zhou, G. Chen, D.J. Singh, and Z.F. Ren, *Energy Environ. Sci.* 10, 799 (2017).
6. Z.W. Chen, Z.Z. Jian, W. Li, Y.J. Chang, B.H. Ge, R. Hanus, J. Yang, Y. Chen, M.X. Huang, G.J. Snyder, and Y.Z. Pei, *Adv. Mater.* 29, 1606768 (2017).
7. T. Zhu, Y. Liu, C. Fu, J.P. Heremans, J.G. Snyder, and X. Zhao, *Adv. Mater.* 14, 1605884 (2017).
8. J.-F. Li, Y. Pan, C.-F. Wu, F.-H. Sun, and T.-R. Wei, *Sci. China Technol. Sci.* 60, 1347 (2017).
9. J.-F. Li, W.-S. Liu, L.-D. Zhao, and M. Zhou, *NPG Asia Mater.* 2, 152 (2010).
10. W.Y. Zhao, Z.Y. Liu, P. Wei, Q.J. Zhang, W.T. Zhu, X.L. Su, X.F. Tang, J.H. Yang, Y. Liu, J. Shi, Y.M. Chao, S.Q. Lin, and Y.Z. Pei, *Nat. Nanotechnol.* 12, 55 (2017).
11. Z.-Y. Li, J.-F. Li, W.-Y. Zhao, Q. Tan, T.-R. Wei, C.-F. Wu, and Z.-B. Xing, *Appl. Phys. Lett.* 104, 113905 (2014).
12. Y. Pan, U. Aydemir, F.-H. Sun, C.-F. Wu, T.C. Chasapis, G.J. Snyder, and J.-F. Li, *Adv. Sci.* 4, 1700259 (2017).
13. Q.F. Chen, Y.C. Yan, H. Zhan, W. Yao, Y. Chen, J.Y. Dai, X.N. Sun, and X.Y. Zhou, *J. Materiomics* 2, 179 (2016).
14. J. Li, Q. Tan, J.-F. Li, D.-W. Liu, F. Li, Z.-Y. Li, M. Zou, and K. Wang, *Adv. Funct. Mater.* 23, 4317 (2013).
15. C.-F. Wu, T.-R. Wei, F.-H. Sun, and J.-F. Li, *Adv. Sci.* 4, 1700199 (2017).
16. A. Kaushik, R. Kumar, S.K. Arya, M. Nair, B.D. Malhotra, and S. Bhansali, *Chem. Rev.* 115, 4571 (2015).
17. T. Barbier, P. Lemoine, S. Gascoin, O.I. Lebedev, A. Kaltzoglou, P. Vaqueiro, A.V. Powell, R.I. Smith, and E. Guilmeau, *J. Alloy Compd.* 634, 253 (2015).
18. Y. Bouyrie, C. Candolfi, V. Ohorodniichuk, B. Malaman, A. Dauscher, J. Tobola, and B. Lenoir, *J. Mater. Chem. C* 3, 10476 (2015).
19. X. Lu, D.T. Morelli, Y. Xia, F. Zhou, V. Ozolins, H. Chi, X. Zhou, and C. Uher, *Adv. Energy Mater.* 3, 342 (2013).
20. K. Suekuni, K. Tsuruta, T. Ariga, and M. Koyano, *Appl. Phys. Express* 5, 051201 (2012).
21. F.-H. Sun, C.-F. Wu, Z. Li, Y. Pan, Asfandiyar, J. Dong, and J.-F. Li, *RSC Adv.* 7, 18909 (2017).
22. R. Chetty, A. Bali, and R.C. Mallik, *J. Mater. Chem. C* 3, 12364 (2015).
23. Y. Bouyrie, M. Ohta, K. Suekuni, Y. Kikuchi, P. Jood, A. Yamamoto, and T. Takabatake, *J. Mater. Chem. C* 5, 4174 (2017).
24. W. Lai, Y.X. Wang, D.T. Morelli, and X. Lu, *Adv. Funct. Mater.* 25, 3648 (2015).
25. F.-H. Sun, J. Dong, S. Dey, Asfandiyar, C.-F. Wu, Y. Pan, H. Tang, and J.-F. Li, *Sci. China Mater.* 61, 1209 (2018).
26. R. Chetty, A. Bali, M.H. Naik, G. Rogl, P. Rogl, M. Jain, S. Suwas, and R.C. Mallik, *Acta Mater.* 100, 266 (2015).
27. J. Callaway and H.C. Vonbaeyer, *Phys. Rev.* 120, 1149 (1960).
28. H.S. Kim, W. Liu, and Z. Ren, *Energy Environ. Sci.* 10, 69 (2017).